

Finite element modeling on the effect of intra-granular porosity on the dielectric properties of BaTiO₃ MLCCs

Graham Dale¹ | Maureen Strawhorne¹ | Derek C. Sinclair²  | Julian S. Dean² 

¹AVX Ltd, Coleraine, County Londonderry, UK

²Department of Material Science & Engineering, University of Sheffield, Sheffield, UK

Correspondence

Julian S. Dean, Department of Material Science & Engineering, University of Sheffield, Sheffield, UK.
Email: j.dean@sheffield.ac.uk

Funding information

Engineering and Physical Sciences Research Council, Grant/Award Number: EP/L017563/1, EP/P019919/1

Abstract

The effect of porosity on the electrical properties of BaTiO₃-based Multilayer Ceramic Capacitors (MLCCs) is studied. A dense ceramic prepared via powder from a solid-state processing route is compared against a ceramic that contains intra-granular pores from powder prepared via hydrothermal processing. Finite element models are created to contain intra-granular pores, solved and analyzed to show an increase in the electric field and current density surrounding the pores. For single-pore and two intra-pore arrangements, the electric field is enhanced by a factor of ~1.5 and 2.5, respectively, when compared to a fully dense (pore-free) material. For ceramics with equivalent density, the number of pores dramatically alters the electrical response. For a system containing 100 pores, the electric field can increase at least fourfold, therefore facilitating a possible starting route for electrical breakdown of the grain. These results are compared to the Gerson-Marshall model, typically used in the literature for the calculation of the breakdown strength due to porosity. The results highlight the need to include the effect of adjacent pore interactions. Although studied here for BaTiO₃-based MLCC's the results are applicable to other devices based on ceramics containing porosity.

KEY WORDS

barium titanate, degradation, finite element analysis, multilayer capacitors, pores/porosity

1 | INTRODUCTION

There are over 2 trillion BaTiO₃-based multilayer ceramic capacitors (MLCCs) produced every year for a variety of applications. Despite this staggering number of components, the electronics market constantly demands higher capacitance and therefore thinner dielectric layered BaTiO₃-based MLCCs for applications (e.g., automotive) that require device reliability at increasingly higher operating temperatures (e.g., >125°C) and voltages (e.g., >25 V). To meet this demand, the thickness of the dielectric layers in MLCCs have been reduced to below 1 micron and the

electrical response of the ceramic layers is therefore dependent on only a few grains of BaTiO₃-based material between each set of internal electrodes. This has been achieved by a combination of using nano-sized starting powders and innovative processing methods. As a consequence, each dielectric layer in an MLCC is exposed to significant dc electric fields and this can lead to fatigue, degradation and ultimately, dielectric breakdown. The electrical response(s) of the dielectric layers is highly dependent on any changes and/or variability in the ceramic microstructure of the dielectric layers and is therefore intimately linked to the starting powders and processing

This is an open access article under the terms of the Creative Commons Attribution License, which permits use, distribution and reproduction in any medium, provided the original work is properly cited.

© 2017 The Authors *Journal of the American Ceramic Society* published by Wiley Periodicals, Inc. on behalf of American Ceramic Society (ACERS)

conditions used during fabrication. Future developments to maintain size-reduction while retaining or improving long-term device reliability depends critically on understanding how changes in microstructure influence the high field electrical properties.

The dielectric properties of BaTiO₃ (BT) ceramics strongly depend on the morphological characteristics of the starting powders, including crystallite size, particle size distribution and the level of agglomeration. The breakdown strength of dielectric materials can be critically affected by various intrinsic and extrinsic factors. Low values are usually attributed to various types of defects, generally arising from the quality of the starting powders and the processing route(s).¹ For example, the breakdown strength typically decreases with increased porosity and grain size.²⁻⁵

One of the widely accepted models relating the effects of porosity on the breakdown strength of porous ceramics is the Gerson-Marshall model,³ where the dielectric strength in porous ceramics is dependent on the porosity and grain size. This model predicts how the breakdown strength of the material decreases from a fully dense bulk value, when porosity is introduced. Both experimental results and theoretical calculations reveal the breakdown strength of ceramics can be reduced by a factor of ~2 if the porosity reaches 10%. A key feature of this model is that the only significant parameter is the number and size of the pores parallel to the applied voltage; however, it does not consider their proximity and interactions in other directions.

Traditionally, BT is prepared by a solid-state (SS) reaction that involves ball milling of BaCO₃ and TiO₂.⁶ The mixture is then calcined at high temperature. BT powders prepared via this solid-state route (SS-BT) can be highly agglomerated, with a large average particle size and can contain high impurity contents due to inherent problems such as high reaction temperature and heterogeneous solid phase reaction.⁷⁻⁹ These have been identified in creating poor electrical properties of sintered SS-BT ceramics; however, processing routes have been substantially improved and it is now possible to fabricate, nano-sized SS-BT powders that are suitable for obtaining high quality, dense SS-BT ceramics.

To eliminate many of the early problems associated with SS-BT powders, a variety of wet chemical synthesis routes have been developed to generate higher purity, homogeneous, reactive ultrafine barium titanate powder at lower temperatures. Aqueous-based Hydrothermal (HT) processing is of great interest because of the possibility of producing highly crystallized, well-dispersed and sintering-active nano-powders at low temperatures.¹⁰⁻¹⁴ Despite these apparent advantages, HT-BT powders can suffer from the presence of structural water during fabrication that can generate significant levels of intra-granular porosity.¹²⁻¹⁴ For

example, it has been demonstrated that short HT reaction times can create small BT particles that contain a large number of small internal pores but with increased HT reaction times, the particles grow and the pores become larger but fewer in number.¹⁴ These pores within the particles of HT powders are attributed to an accumulation of point defects, primarily associated with the presence of hydroxyl groups that can replace oxygen ions in the BT lattice on the surfaces of the internal pores. Combined with the presence of protons, the internal pores act as a form of structural water that is not removed (i.e., dehydration) until powders are heated above ~700°C,¹⁴ therefore creating intra-granular pores in the grains of sintered HT-BT ceramics.

Here, we use a combination of finite element modeling (FEM) and experimental results from sets of MLCCs fabricated from both HT- and SS-BT powders to elucidate the influence of intra-granular porosity on the electrical properties of these devices.

2 | EXPERIMENTAL METHODOLOGY AND RESULTS

Two different BT-based MLCCs have been fabricated and analyzed at AVX (Coleraine). Two lots of MLCCs with dimensions of 0.30 × 0.15 mm were fabricated, each with 4.6 micron dielectric layers. Lot A was fabricated using a SS-BT source powder while Lot B was based on a HT-BT source powder. Simultaneous incorporation of minor dopants and additives were employed to achieve X7R capacitor temperature stability (TCC). The MLCCs used 230 electrodes and fired at temperatures exceeding 1200°C, in a reducing atmosphere typically controlled by H₂, N₂, O₂ and H₂O, (\log_{10} pO₂ (atm) ~−16 to −19). The ceramic microstructure of the dielectric layers in the MLCCs were studied by scanning electron microscopy (SEM) using a MIRA3, TESCAN. A highly accelerated life-test (HALT) method was employed to establish life reliability for both lots, all measured to failure. Each lot tested over 30 MLCCs using a voltage of 142 V applied at an elevated temperature of 150°C.

SEM images show the variations in grain size and shape between the two sintered materials is not significantly different. An SEM image of a layer of the SS-BT based MLCC highlights a typically granular structure, Figure 1A. The average grain size was measured to be ~0.2 μm for SS-BT, Figure 1A and ~0.3 μm for HT-BT based devices, Figure 1B; however, larger grains were present in both samples. The SS-BT layers are relatively dense with no discernible volume of intra-granular pores, whereas the grains in the HT-BT layers clearly contain a significant volume of intra-granular pores.

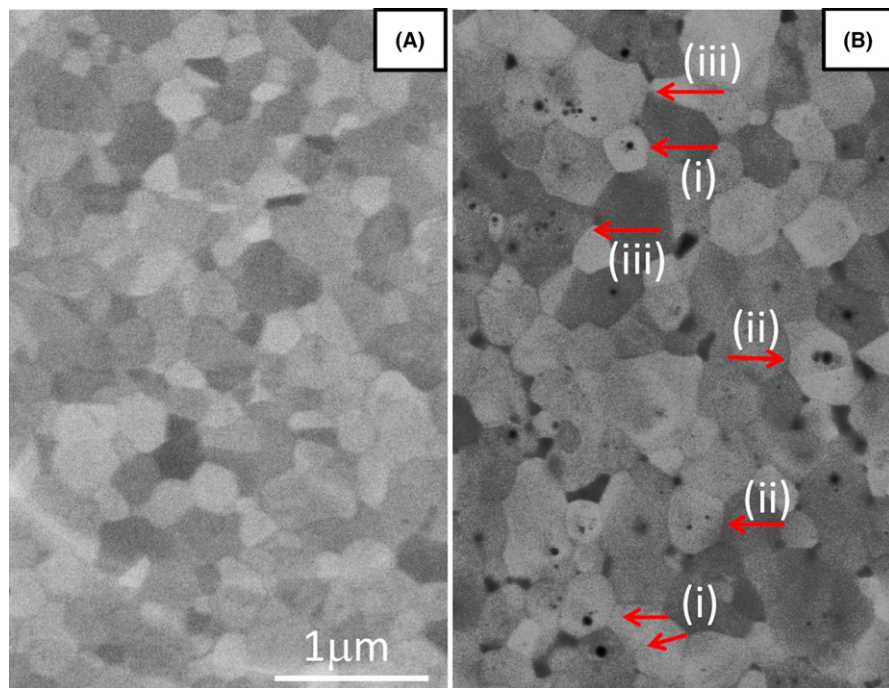


FIGURE 1 SEM images of (A) solid-state and (B) hydrothermal-based BaTiO_3 ceramic as part of a layer within an X7R MLCC. A selection of hydrothermal grains is annotated for clarity to show different features within single grains; (i) a large, single intra-granular pore; (ii) two intra-granular pores; and (iii) multiple smaller pores

Three types of intra-granular pores are observed in Figure 1B. Type, (i) where a single grain contains one large pore. The location of this can vary and in some cases may be located towards the edge of the grain surface. These single pores generally appear to be large, taking up a significant fraction of the grain volume. Type (ii) show that two pores can be created that are close together, while the distance and orientation between these two pores, in relation to the placement of the electrode, varies. Finally type (iii) highlights where a grain contains many smaller intra-granular pores. These appear to be smaller pores but are distributed throughout the grain.

The implications of these intra-grain pores for industrial applications can be highlighted when the lifetime of MLCC components are fabricated from layers of these materials. Figure 2A shows a typical resistance-time HALT profile for a single MLCC from each set. In this case, the HT-BT based device has a higher initial resistance of $\sim 4 \text{ M}\Omega$ but it quickly drops and fails approximately 6 hours into the test. The SS-BT based component has a different profile, starting with a lower resistance of $\sim 2.2 \text{ M}\Omega$ but with a marked increase in lifetime to over 16 hours. As the resistance falls to zero, the lifetime of the component is recorded. As shown in Figure 2B this can vary, however, typically the SS-BT leads to a greater lifetime when compared to the HT-BT based MLCC. Although both profiles are reasonably similar, the slope of the cumulative failures is rather different and therefore suggests the origin of breakdown is different in both cases. Understanding the role of intra-granular porosity in the dielectric layers on the failure of

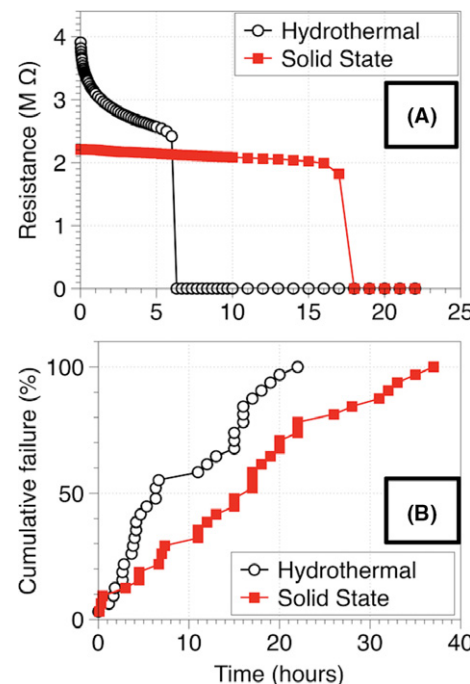


FIGURE 2 Typical time-dependent resistance profiles for both materials based on an accelerated lifetime test (HALT) conducted using 142 V at 150°C. (A) shows a typical resistance profile comparison between a MLCC made from solid-state (SS) and hydrothermal (HT) BT. (B) The percentage cumulative failure vs time made from solid-state (SS) and hydrothermal (HT) BT

an MLCC is therefore critical in understanding how components behave and how to achieve improvements to enhance device lifetime.

3 | MODELING METHODOLOGY

To simulate the effect of pores on the electrical properties in grains we use an in-house developed FEM package, Elcer, to predict the electrical response of the electro-ceramic materials.¹⁵⁻¹⁷ This package incorporates a time domain finite element method (TDFEM) to solve Maxwell's equations in space and time. We combine a realistic microstructure of the system to form individual volumes, where each electrically active region can be assigned its own unique properties. The model is then meshed using Gmsh¹⁸ and solved using Elcer. These different regions possess an individual conductivity (σ) and relative permittivity (ϵ_r) simulating an electrical heterogeneity within the model without the need for equivalent circuits and constant phase elements.

We simplify the model to study the effect of pores on the HT material by studying the response of an individual grain. We assume a cubic grain of $1 \mu\text{m}^3$ where the pores are located internally as spherical objects. The center of the cube is set as the origin and the cube extends from -0.5 to $0.5 \mu\text{m}$ along each axis. A constant potential difference of 142 V is applied across the top and bottom surfaces of the grain, aligned to the z -axis, thus simulating the HALT conditions. The response of the system is taken once the current flow reaches a static equilibrium. We apply material properties of $\sigma = 2.5 \times 10^{-8} \text{ Sm}^{-1}$ and $\epsilon_r = 3681$ that replicate the HT-BT ceramic at 150°C (with no dc bias) as measured from a combination of impedance spectroscopy and fixed frequency permittivity measurements (data not shown). The pore is assigned the properties of typical air¹⁹ with $\sigma = 0.5 \times 10^{-14} \text{ Sm}^{-1}$ and $\epsilon_r = 1$.

A single $1 \mu\text{m}^3$ HT-grain using these properties generates a resistance of $40 \text{ T}\Omega$ and an internal uniform electric field of 142 MVm^{-1} when a potential difference of 142 V is applied across the contacts. To provide comparison to other geometry and material properties, the results are

normalized to this homogenous case. The normalized values are used as comparison throughout and leads to the normalized electric field (E_n), current density (J_n) and resistance (R_n) being unity for a fully dense HT-BT grain.

3.1 | Single intra-grain pore response

We first design and simulate a single internal pore in a grain. To achieve this, we create a sphere assigned as a pore at the centre of a cubic grain, Figure 3A. We control the radius, increasing it from 0.005 to $0.49 \mu\text{m}$ leading to a reduction in grain density to 50.7% .

The normalized grain resistance (R_n) and maximum electric field ($E_{n,\max}$) both increase with the pore size, Figure 3B. The existence of the smallest pore generated (5 nm) initially generates an increased $E_{n,\max}$ within the pore of a factor of 1.5. As the pore size increases $E_{n,\max}$ remains relatively constant at 1.5 until the pore radius increases to $0.5 \mu\text{m}$ (equivalent to a 52% dense grain) where it dramatically rises to a factor of 2.5 and beyond. R_n rises by a similar factor as the volume of the pore rises to 50% of the total volume (representing a 52% dense grain). At small pore sizes, however, less than 5% of the grain volume, no resistance change is detectable.

In addition to assessing the extrinsic electric properties associated with incorporation of pores, Elcer also allows the internal electrical microstructure to be probed. Figure 4A-C show a central cut through pores of radius 0.1 , 0.2 , and $0.48 \mu\text{m}$, respectively, and are displayed with a color coding for the electric field profile. A streamline analysis is overlaid on the model to highlight the direction and intensity of the electric field vector. Where lines are close, the field is constricted and therefore generates inhomogeneous electrical behavior. The stream trace is found to be similar for both the current density and electric field profiles but highlights different phenomena.

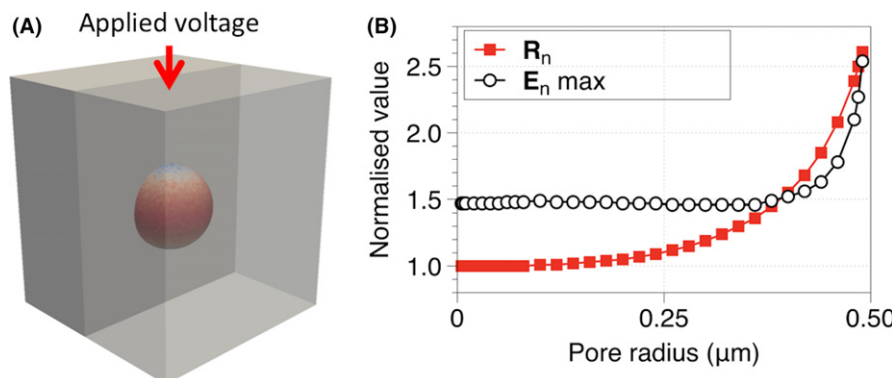


FIGURE 3 (A) A slice through a 3D model representing a single intra-granular pore of radius $0.10 \mu\text{m}$ inside a $1 \mu\text{m}^3$ grain giving rise to a grain density of 96.6%; (B) the normalized maximum electric field factor ($E_{n,\max}$) and normalized resistance (R_n) as a function of pore radius. These values were normalised against those measured for a fully dense sample

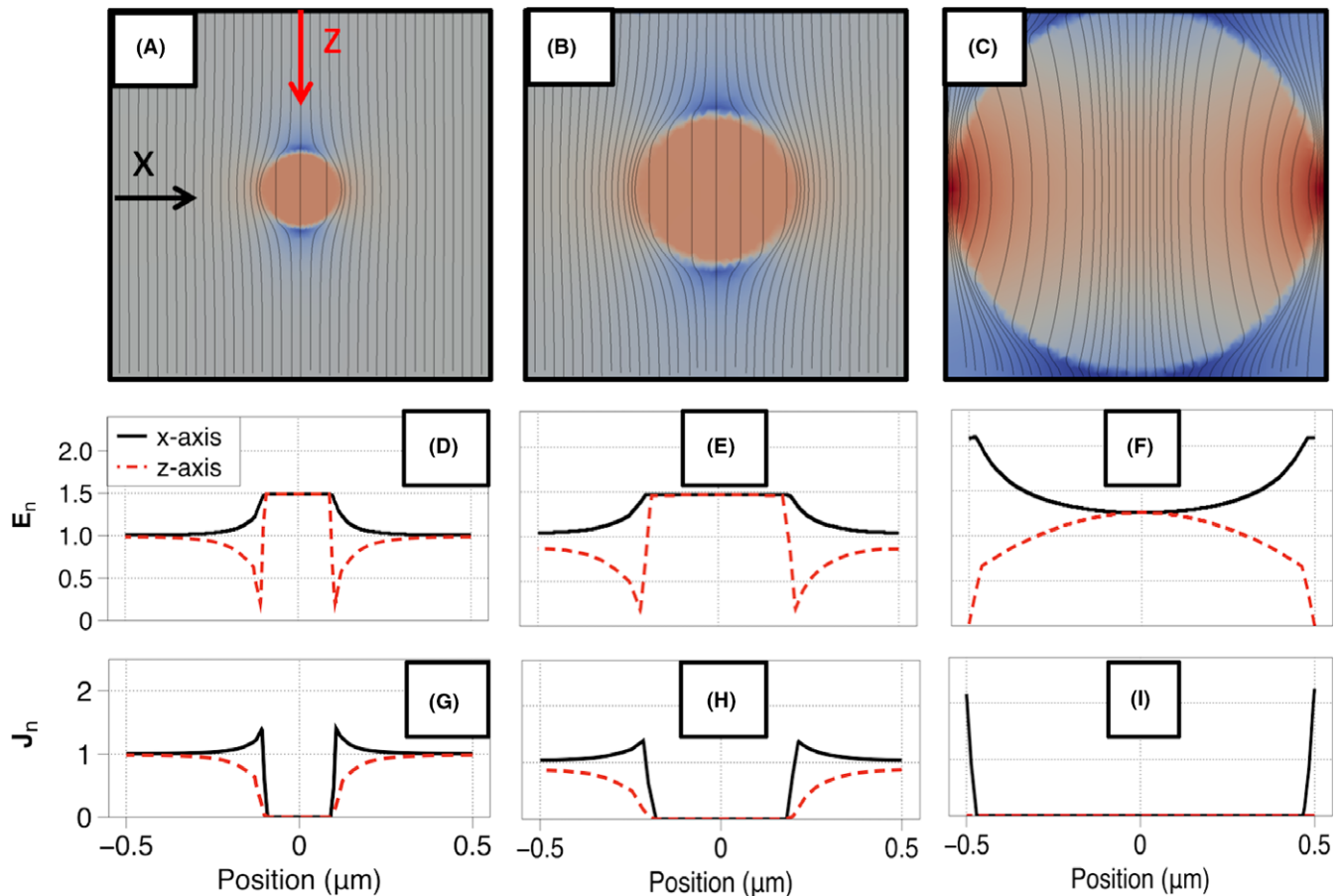


FIGURE 4 The size effect of a single intra-granular pore on the normalized electric field (E_n) and current density (J_n) profiles for a pore radius of 0.10 (A, D, G), 0.20 (B, E, H) and 0.48 μm (C, F, I) giving rise to grain densities of 99.6%, 96.6% and 53.7%, respectively. Parts (A-C) show a central 2D slice through the solved 3D model and highlight a stream trace and color of the electric field generated where red and blue indicate high and low fields, respectively. Parts (D-F) and (G-I) show E_n and J_n through the centre of the pore for the various radii. These are provided parallel and perpendicular to the applied voltage, z- and x-axes, respectively

For a pore radius of 0.10 μm (grain density 99.6%), shown in Figure 4A, the field flows around the pore avoiding the resistive path through it, as shown by the near zero current density inside the pore. There is an increased flow of current around this region, increasing to a factor of 1.5. This also generates a reduction in the electric field, above and below the pore in the direction of the applied voltage as shown along the z-axis in Figure 4D. Of greater significance is the increase in electric field around the sides of the pore by a factor of 1.5 perpendicular to the current flow, as shown in Figure 4D. This increased electric field remains relatively constant as the pore size increases until the pore begins to interact with the sides of the grain. At this point, the surface of the box and the pores surface begin to interact causing the current to be squeezed through the narrow region between the pore and grain surfaces. This creates a constriction resistance, increasing the resistance of the system by over twice that of the unrestricted case shown in Figure 4I. A similar increase in the electric field is also created in Figure 4C,F.

3.2 | Interacting pores

Experimentally, whilst some grains possess a single internal pore, there are many grains where two or more pores are located close together. To simulate how these interact, we fix a pore radius of 0.10 μm and align two intra-granular pores such that their centers are positioned either along an axis perpendicular (Figure 5) or parallel (Figure 6) to the applied voltage along the z-axis. We create a set of models altering the distance between them from 0.01 to 0.30 μm ensuring the pores do not interact with the surface of the grain. This is to ensure the effects observed arise only from the pore-pore interaction.

If the pores are located perpendicular to the field, the current is forced around them as shown in Figure 5A-C. This can dramatically increase the electric field by a factor of 2.5, when they are close together as in Figure 5D. This is due to some of the current being directed and squeezed between the two pores. An associated constriction resistance is also observed in Figure 5G with an observed spike in the current density between the pores.

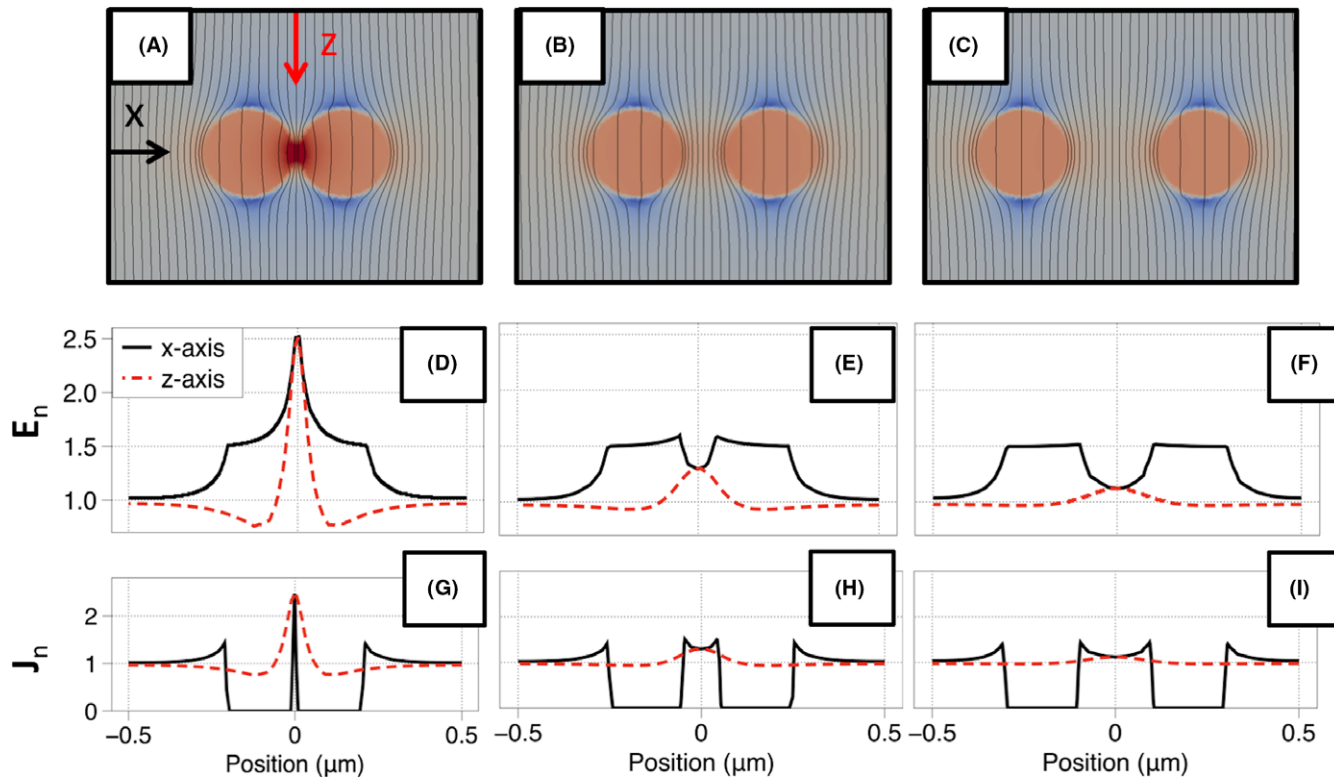


FIGURE 5 The effect of distance on the normalized electric field (E_n) and current density (J_n) profiles for two perpendicular intra-granular pores with respect to the applied voltage. The profiles are shown for a pore of radius 0.10 μm , with a distance between the pores of 0.01 (A, D, G) 0.10 (B, E, H) and 0.20 μm (C, F, I). Parts (A-C), (D-F), and (G-I) show a central 2D slice through the various distances, with an overlaid stream trace. The electric field colour of red and blue indicate high and low fields, respectively. The fields are measured both parallel and perpendicular to the applied voltage, z - and x -axes, respectively

If the pores are orientated parallel to the field the behavior is different. If they are close together the current cannot flow between them and they effectively act as a single large pore, shown in Figure 6D,G, and are comparable with the field profiles in Figure 4. The electric field between them is reduced almost to zero. As seen from the current density profiles, the width of the reduced current density is also different along the two directions. Along the x -axis the width of the pores is similar to that of an individual pore, whereas in the z -axis it extends twice as much. This indicates a stagnation point in the field flow arising due to one pore shielding the response of the other. The effective size of the combined pores in the current direction is thus dependent upon the pore profile along the z -axis, consistent with the Gerson-Marshall model.³

As the pores separate, they begin to act independently again, behaving as two single pores, Figure 6C. An associated increase in current density and electric field is observed between them converging towards unity.

These two orientations are compared in Figure 7. Here, the normalized electric field generated by these models is plotted as a function of the distance between the pores. At approximately 0.40 μm , four times the pore radius, the electric field returns to unity, indicating that the pores can once again be

treated as non-interacting defects. This trend is also observed for the current density and for other pore sizes (not shown).

Experimentally, there appears no trend to the orientation of the pores in the grain with respect to the applied voltage, Figure 1. To study what affect this may have, we continue with two pores of radius 0.10 μm but set at a fixed center-to-center distance apart of 0.15 μm . This provides a factor of 1.3 that allows us to observe the effect as a function of pore orientation. As shown in Figure 8A we start with the angle between both pores of 0°, aligning the pores perpendicular to the applied voltage as shown in Figure 8B. They are then rotated around their centre to an angle of 90°, aligning the pores parallel to the applied voltage as shown in Figure 8E.

At 0°, we observe the typical constriction and an associated increase in the electric field by a factor of 1.3. As they rotate, this reduces quickly to less than a factor of 1.1 at 40° with the corresponding model shown in Figure 8D. At this point, the pores begin to generate a “shielding” effect that reduces the constriction factor back to unity as the current flows around both of them and they now begin to act as a single, larger pore. Thus, orientation of the pores with respect to the applied voltage is a significant factor in ceramic microstructures.

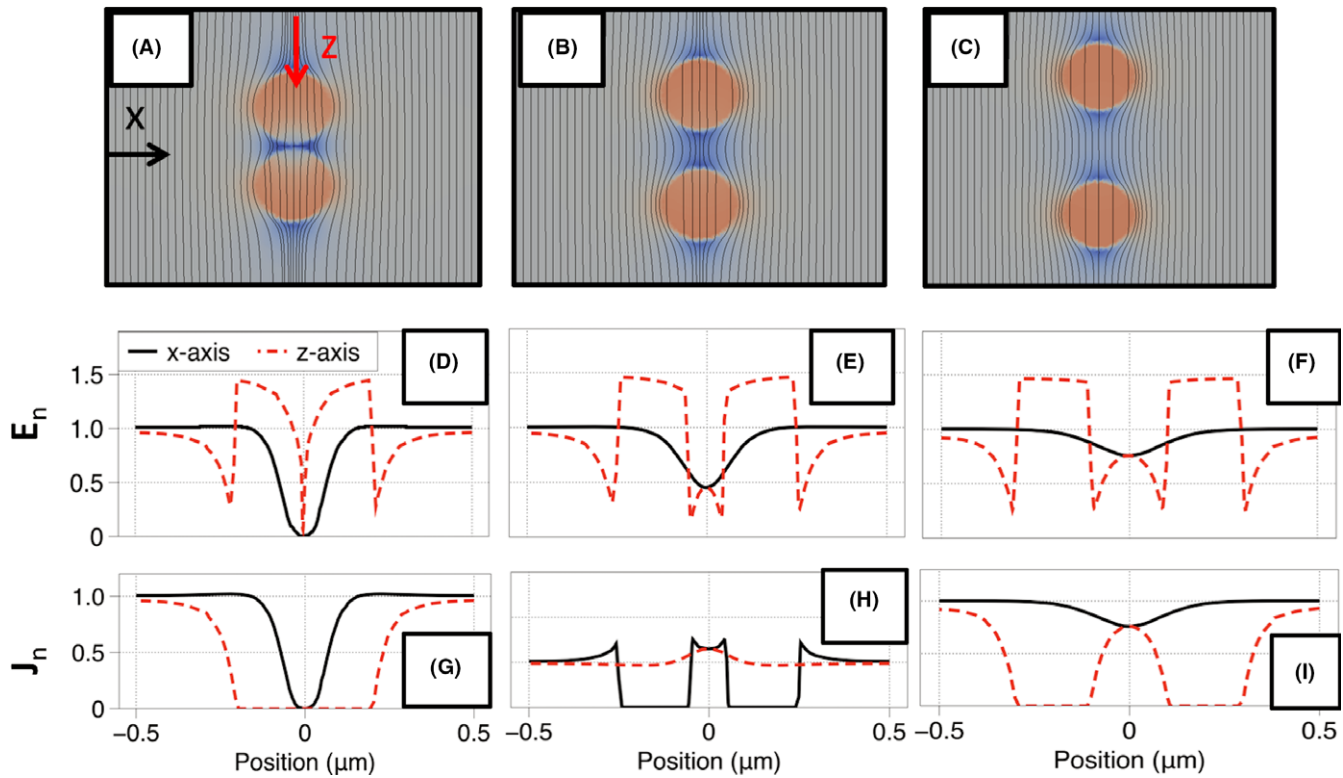


FIGURE 6 The effect of distance on the normalized electric field (E_n^F) and current density (J_n^F) profiles for two parallel intra-granular pores with respect to the applied voltage. The profiles are shown for a pore of radius 0.10 μm , with a distance between the pores of 0.01 (A, D, G) 0.10 (B, E, H) and 0.20 μm (C, F, I). Parts (A-C), (D-F), and (G-I) show a central 2D slice through the various distances, with an overlaid stream trace. The electric field colour of red and blue indicate high and low fields, respectively. The fields are measured both parallel and perpendicular to the applied voltage, z- and x-axes, respectively

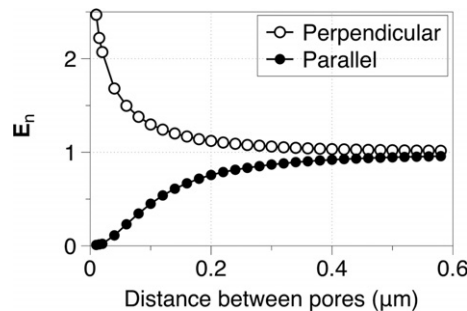


FIGURE 7 The effect of the normalized electric between the pores as a function of the distance between them and their orientation. A convergence towards the value of a homogenous grain is observed at approximately 0.4 μm in both cases, approximately four times the radius of the individual pores. A similar profile is observed for the current density

3.3 | Multiple pores

The maximum electric field generated from systems with intra-granular pores can vary dramatically depending on its location, size, and distance to neighboring pores. Experimentally there can be a mixture of grains in a dielectric

based on those without pores to those with single pores, a few pores or many small pores, Figure 1B.

As shown for the single and double interacting pore case scenarios, the increase in electric field can be significant and as such we use our FEM to understand its possible significance for multi-pore systems. Each model has a fixed overall density but the number of pores present is varied. We randomly place the pores into the grain, treating them as hard spheres to avoid any overlap. This is shown in Figure 9A for an 85% dense grain with 100 identical pores. Due to the large variation in configurational positions, we run 100 random configurations and average the results. When many pores are present in a grain, there is a significant chance that some pores are very close together in different orientations, as shown in Figure 9B which is taken from a slice of Figure 9A. This one slice contains many pores that appear not to be interacting but two regions are highlighted for interest. Near the top left (i), two pores have a highly elevated electric field and a large electric field is generated in the model. This arises as the two pores are close together, parallel to the applied voltage, causing a high constriction resistance between them. Located at the bottom left (ii) are two pores close together

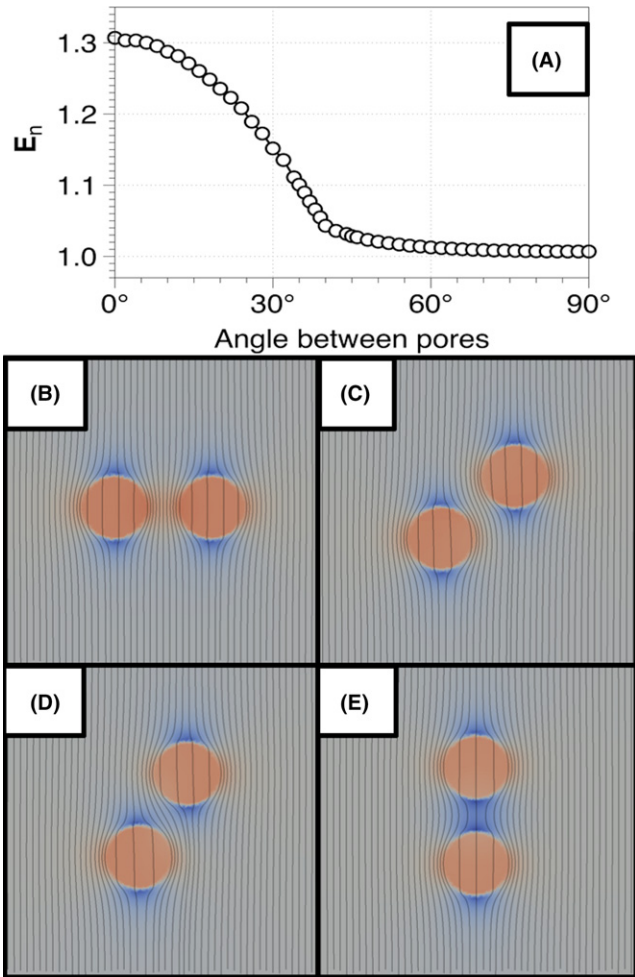


FIGURE 8 The effect of E_n versus orientation for two intra-granular pores of radius $0.10\text{ }\mu\text{m}$ in single grain, set at a distance of $0.10\text{ }\mu\text{m}$ apart. Their orientation is rotated from orthogonal to the applied voltage at angles of (B) 0° , (C) 20° , (D) 45° , and (E) 90° . A stream trace and colour of the electric field is overlaid where red and blue indicate high and low fields, respectively

but due to their orientation they have a reduced electric field between them.

As the grain density increases (i.e., the total volume fraction of pores decreases) the average electric field in the grain decreases, Figure 9C. Of more significance is the increase in electric field with an increasing number of pores for a fixed grain density, Figure 9C. This suggests (for a fixed grain density) that a reduction in the breakdown strength in a ceramic is more likely to occur where there is a large number of intra-granular pores.

To highlight the significance of pore interactions revealed by our FEM model we compare this to the Gerson-Marshall model³ (where pore interactions are not considered) to estimate the normalized breakdown strength reduction that arises from changes in porosity and pore-size. To provide a better comparison to the FEM model, we assume the breakdown

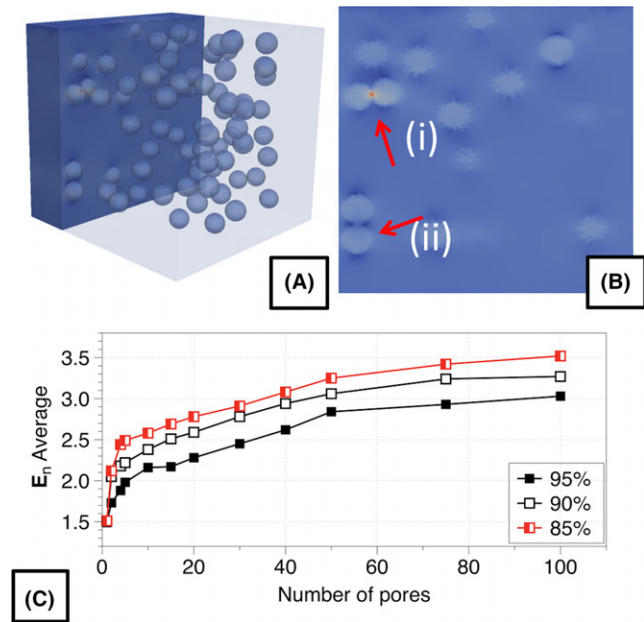


FIGURE 9 A multi-intra-granular model that ranges from containing a single large pore to 100 small pores. The size of the pore is controlled to achieve a specific grain density. Part (A) a slice of an 85% dense grain with 100 pores with (B) showing a 2D slice of E_n , highlighting how the orientation of the pores can lead to high and low electric fields. Part (C) the average normalized electric field (E_n , av) vs the number of pores for three values of grain density

strength of the material is set as unity for a fully dense sample. This allows us to create a prediction from the FEM of the normalized breakdown strength. Both models have been tested for set densities of 85%, 90% and 95% and both show the density significantly influences the breakdown strength, Figure 10. For a small number of pores, the Gerson-Marshall model shows a reduction in the normalized breakdown strength from ~ 0.65 for 5% porosity to < 0.5 for 15% porosity, Figure 10A. However, if the pore size is decreased (therefore increasing the number of pores forming the porosity) the normalized breakdown strength appears to partially recover and increase to ~ 0.7 and ~ 0.5 for 5% and 15% porosity, respectively, Figure 10A. This is due to the underlying assumption in the model that breakdown will occur along a purely parallel pathway (i.e., column) in the direction of the applied voltage that contains the maximum number of pores and therefore a minimum amount of ceramic material. There is no consideration of pore interactions along the perpendicular directions and/or between adjacent “columns”. As the pore size decreases, the probability of a large number of pores located in any one parallel column decreases and therefore the breakdown strength partly recovers.

For the FEM model a similar trend in the reduction in normalized breakdown strength with decreasing grain density is observed for a few pores; however, in contrast to

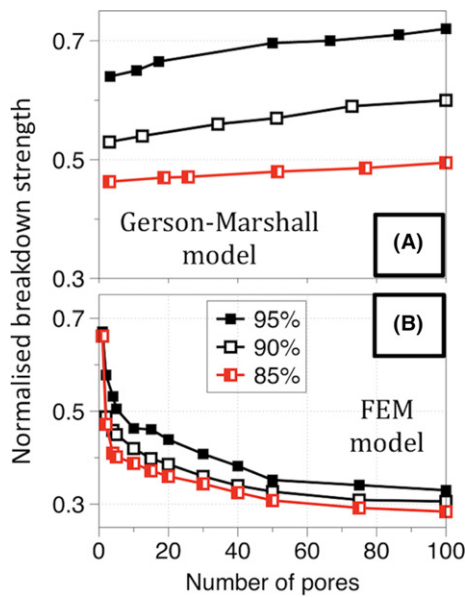


FIGURE 10 A comparison of the reduction in the normalized breakdown strength calculated using (A) the Gerson-Marshall model and (B) our FEM model. Three densities are solved, modifying the pore-size to alter the number present in the model. Both models show the breakdown strength increases with increasing grain density; however, the Gerson-Marshall model shows as the number of smaller pores increases the breakdown strength of the material increases, whereas the FEM shows a further reduction in the breakdown strength due interactions between neighbouring pores

the Gerson-Marshall model, the normalized breakdown strength for a fixed grain density decreases with an increasing number of pores, Figure 10B. For all three grain densities, the normalized breakdown strength decreases significantly to a final value of ~0.28–0.35, Figure 10B. This trend occurs due to enhanced electric fields occurring between adjacent interacting pores.

For example, if the density of a grain is set at 85% due to the presence of a large single pore, the normalized electric field E_n rises from 1 to 1.5, with a normalized breakdown strength reducing to ~0.65. However, if the same grain density is generated from 100 smaller pores, the maximum normalized electric field $E_{n,max}$ increases on average to 3.5 with maximum values in some configurations generating factors in excess of 4. This reduces the normalized breakdown strength to <0.3. This increase in electric field value is over twice that which can be created from just two very closely positioned pores. It is therefore important to take account of the proximity of the pores to one another in addition to the total number of pores.

For a typical 1 μm grain with 1 V applied across it, this would cause the electric field to rise to 4 MV m^{-1} . This value is higher than the 3 MV m^{-1} typically used as the breakdown strength of air.²⁰ This suggests that under these conditions the grain could experience an electrical short

TABLE 1 Summarizes how the grain density and number of physical pores present influences the average, normalized electric field ($E_{n,av}$) and reduction in the breakdown strength. The number of grains exceeding the breakdown strength of air is estimated for a 1 μm grain with an applied voltage of 1 V

Density	Number of pores	$E_{n,av}$ (standard deviation)	Grains exceeding breakdown (%)		Normalised breakdown strength
			(%)	(%)	
100	0	1 (0)	0	0	1.00
95	5	1.63 (0.2)	0	0	0.50
95	100	2.89 (0.62)	13	0	0.33
85	5	2.38 (0.48)	0	0	0.40
85	100	3.5 (0.64)	46	0	0.28

through the pores and thus provide a possible route for dielectric breakdown of the grain and therefore the device.

From 100 simulations of an 85% dense grain using 100 randomized pores, the generated electric field factors varied significantly with an average of 3.4 and a standard deviation of 0.64. For a 1 μm grain with a 1 V potential applied, this would correspond to 46% of grains exceeding the breakdown strength of air. If the same grain density was created from only 5 pores, no grains would exceed the breakdown strength of air but would still possess a high average of 2.38 with a standard deviation of 0.48. There is a similar trend for a 95% dense grain with 13 grains reaching this critical value for 100 pores (average 2.89, SD 0.62) and no grains reaching this critical value for 5 pores (average 1.63, SD 0.2). This is summarized in Table 1. This electric field enhancement and distribution is attributed to the increased probability that pores are located closer to each other, therefore generating a greater constriction of the electric field. It also highlights a limitation of the Gerson-Marshall model based on the assumption that only the number of pores located in a purely parallel direction should be considered. It should also be noted, however, that the overall resistance of the models is relatively independent of the number of pores.

Linking these findings back to the experimental observations, for the HT-BT based MLCC device shown in Figure 1B, while most of the grains possess one or two pores, some grains possess many intra-granular pores. The electric field concentration would be greatest in these grains and therefore most likely to influence the electrical microstructure. The electric field concentration in such grains could not only cause breakdown in a number of these pores but could induce significant migration of point defects towards or away from these regions (depending on their charge), therefore altering the local material properties within such grains. Consequently, this could influence the electrical microstructure and cause a rapid degeneration of the

material and ultimately lead to failure. In the case of the SS-BT based MLCC device shown in Figure 1A, the more homogeneous ceramic microstructure with negligible intra-granular pores is much less susceptible to such an electric field concentration phenomenon. Electrical breakdown of this material would most likely arise from a different process/mechanism. This is supported with the different HALT profiles for the two devices in Figure 2 and further work is underway to study this in more detail.

ACKNOWLEDGMENTS

We thank the Engineering and Physical Science Research Council (EPSRC) for funding (EP/L017563/1; Substitution and Sustainability in Functional Materials and Device; DCS and JSD, and EP/P019919/1; Charging Ahead with Multi-Layer Ceramic Capacitor Materials; JSD). Mr. Philip Foeller for permittivity and conductivity values for BT ceramics made from the HT-BT source powders used in the fabrication of the HT-BT MLCCs. The Authors also wish to thank Dr. C. L. Freeman for useful discussion.

ORCID

Derek C. Sinclair  <http://orcid.org/0000-0002-8031-7678>
Julian S. Dean  <http://orcid.org/0000-0001-7234-1822>

REFERENCES

1. Liebault J, Vallayer J, Goueriot D, et al. How the trapping of charges can explain the dielectric breakdown performance of alumina ceramics. *J Eur Ceram Soc.* 2001;21:389-397.
2. Dai HY, Liu HZ, Du JF, et al. Effect of sintering temperature on the microstructure, electrical, and magnetic properties of $\text{Bi}_{0.85}\text{Eu}_{0.15}\text{FeO}_3$ ceramics. *J Supercond Nov Magn.* 2014;27:2105.
3. Gerson R, Marshall TC. Dielectric breakdown of porous ceramics. *J Appl Phys.* 1959;30:1650-1653.
4. Zeng T, Lou Q, Bai Y, Dong X, Wang Y, et al. The dielectric breakdown properties of porous PZT95/5 ferroelectric ceramics. *Ferroelectrics.* 2015;478:118-126.
5. Economos G. *The Effect of Microstructure on the Electrical and Magnetic Properties of Ceramics*. New York: John Wiley & Sons; 1958:201-212.
6. Vijatovic MM, Bobic JD, Stojanovic BA. History and challenges of barium titanate: part I. *Sci Sinter.* 2008;40:155-165.
7. Boulos M, Guillemet-Fritsch S, Mathieu F, et al. Hydrothermal synthesis of nanosized BaTiO_3 powders and dielectric properties of corresponding ceramics. *Solid State Ion.* 2005;176:1301-1309.
8. Haertling GH. Ferroelectric ceramics: history and technology. *J Am Ceram Soc.* 1999;82:797-818.
9. Kong LB, Ma J, Huang H, et al. Barium titanate derived from mechanochemically activated powders. *J Alloys Comp.* 2002;337:226-230.
10. Wada S, Suzuki T, Noma T. Preparation of barium titanate fine particles by hydrothermal method and their characterisation. *Jpn Ceram Soc.* 1995;103:1220-1227.
11. Clark II, Takeuchi T, Ohtori N, et al. Hydrothermal synthesis and characterisation of BaTiO_3 fine powders: precursors, polymorphism and properties. *J Mater Chem.* 1999;9:83-91.
12. Hennings DFK, Metzmacher C, Schreinemacher BS. Defect chemistry and microstructure of hydrothermal barium titanate. *J Am Ceram Soc.* 2001;84:179-182.
13. Pithan C, Hennings D, Waser R. Progress in the synthesis of nanocrystalline BaTiO_3 powders for MLCC. *Int J Appl Ceram Tech.* 2005;2:1-14.
14. Baek C, Wang JE, Moon S, et al. Formation and accumulation of intragranular pores in the hydrothermally synthesized barium titanate nanoparticles. *J Am Ceram Soc.* 2016;99:3802-3808.
15. Dean JS, Foeller PY, Reaney IM, et al. A resource efficient design strategy to optimise the temperature coefficient of capacitance of BaTiO_3 -based ceramics using finite element modelling. *J Mater Chem A.* 2016;4:6896-6901.
16. Dean JS, Harding JH, Sinclair DC. Simulation of impedance spectra for a full three-dimensional ceramic microstructure using a finite element model. *J Am Ceram Soc.* 2014;97:885-891.
17. Heath JP, Dean JS, Harding JH, Sinclair DC. Simulation of Impedance Spectra for Core-Shell Grain Structures Using Finite Element Modeling. *J Am Ceram Soc.* 2015;98:1925-1931.
18. Geuzaine C, Remacle J-F. Gmsh: a three-dimensional finite element mesh generator with built-in pre- and post-processing facilities. *Int J Numer Methods Eng.* 2009;79:1309-1331.
19. Pawar SD, Murugavel P, Lal DM. Effect of relative humidity and sea level pressure on electrical conductivity of air over Indian Ocean. *J Geophys Res.* 2009;114:2156-2202.
20. Rigden JS. *Macmillan Encyclopedia of Physics*. New York, NY: Simon and Schuster Macmillan; 1996.

How to cite this article: Dale G, Strawhorne M, Sinclair DC, Dean JS. Finite element modeling on the effect of intra-granular porosity on the dielectric properties of BaTiO_3 MLCCs. *J Am Ceram Soc.* 2017;00:1-10. <https://doi.org/10.1111/jace.15261>